Chinese Chemical Letters 36 (2025) 109801

Contents lists available at ScienceDirect

Chinese Chemical Letters

journal homepage: www.elsevier.com/locate/cclet

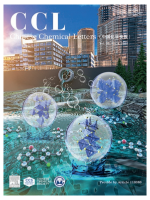

Enhanced electrochemical performance of lithium-rich layered oxide materials: Exploring advanced coating strategies

Bing Jiang[a], Gang Zou[a], Bi Luo[a], Yan Guo[a], Jingru Li[a], Wendi Zhang[a], Qianxiao Fan[a], Lehao Liu[a], Lihua Chu[a], Qiaobao Zhang[b,*], Meicheng Li[a,*]

[a] State Key Laboratory of Alternate Electrical Power System with Renewable Energy Sources, School of New Energy, North China Electric Power University, Beijing 102206, China
[b] State Key Laboratory of Physical Chemistry of Solid Surfaces, College of Materials, Xiamen University, Xiamen 361005, China

ARTICLE INFO

Article history:
Received 31 January 2024
Revised 17 March 2024
Accepted 20 March 2024
Available online 21 March 2024

Keywords:
Lithium-ion battery
Lithium-rich layered oxide materials
Spinel phase
Conductive polymer
Coating

ABSTRACT

In the field of lithium-ion battery cathode materials, lithium-rich layered oxide materials have garnered significant attention due to their exceptional discharge specific capacity and high operating voltage. However, their limitations in terms of cycling stability and rate capability remain major impediments to their wider application. In this study, an innovative approach was employed by simultaneously utilizing the acidic and oxidative properties of phosphomolybdic acid to generate a spinel structure and *in-situ* coating of a conductive polymer (polypyrrole) on the surface of lithium-rich layered oxide materials. This strategy aimed to mitigate structural degradation during charge-discharge cycles, enhance the ionic/electronic conductivity, and suppress side reactions. Experimental results demonstrated that after 200 cycles at a current density of 1 C, the modified sample exhibited a discharge specific capacity of 193.4 mAh/g, with an improved capacity retention rate of 83.3% and a minimal voltage decay of only 0.27 V. These findings provide compelling support for the development and application of next-generation high-performance lithium-ion batteries.

Lithium-ion battery is a type of energy storage device with high energy density and long service life. Since its first successful commercialization in 1991, lithium-ion battery has been widely used in portable electronic devices, aerospace, and other fields. In recent years, its development and application in electric vehicle power systems have seen rapid growth [1,2]. However, with the transformation of the energy structure pursued by society, energy storage has become increasingly important. Current lithium-ion battery is gradually unable to meet the growing demand for energy density, and huge social demand and economic benefits have driven us to begin researching and developing the next generation of high-energy-density lithium-ion batteries [3]. Therefore, developing advanced cathode materials with higher specific capacity is of great significance for improving the energy density of lithium-ion batteries. In this context, lithium-rich layered oxide (LLO) materials with high specific capacity (>300 mAh/g) and high energy density (>1000 Wh/kg) have naturally become the most promising cathode candidates [4,5].

Lithium-rich layered oxide materials are generally considered to be composites of $LiTMO_2$ and Li_2MnO_3 [6], and their formula can be written as $xLi_2MnO_3\cdot(1-x)LiTMO_2$ (TM = Mn, Ni, Co, Al). Although lithium-rich layered oxide materials possess powerful advantages such as high specific discharge capacity, energy density, and wide operating voltage range that are difficult for other cathode materials to match, they suffer from drawbacks such as large initial irreversible capacity loss, poor rate performance, and poor cycle stability [7,8], which hinder their commercial development. During the initial charging process of lithium-rich layered oxide materials, electrochemical activation occurs at voltages above 4.5 V (*versus* Li/Li^+), and Li^+ is deintercalated from Li_2MnO_3, while O^{2-} undergoes a reduction reaction to form O_2^{2-} or O^-, which can provide additional capacity. This is the reason why lithium-rich materials have higher capacity than other cathode materials. However, in the first charge-discharge cycle, there is a large irreversible capacity and low Coulombic efficiency [9]. For the reduction reaction of O^{2-}, some teams have conducted detailed research [10]. Some researchers believe that O^{2-} loses one electron to form an O_2^{2-} dimer, and the O_2^{2-} dimer inside the lithium-rich material can reversibly participate in the charge-discharge cycle. However, the O_2^{2-} dimer on the surface of the material is highly reactive and can undergo side reactions with the electrolyte. At the same time, the

---

[*] Corresponding authors.
E-mail addresses: zhangqiaobao@xmu.edu.cn (Q. Zhang), mcli@ncepu.edu.cn (M. Li).

https://doi.org/10.1016/j.cclet.2024.109801
1001-8417/

loss of O_2^{2-} dimers on the surface of the material can create oxygen vacancies on the particle surface, leading to the rearrangement of internal transition metal ions in the material and the transformation of the layered structure to a spinel structure [11,12]. In subsequent charge-discharge cycles, structural degradation will gradually evolve from the surface to the bulk phase, which can cause the battery to exhibit severe capacity fade and voltage fade [13,14].

To alleviate issues such as oxygen loss, transition metal migration, and structural degradation, researchers have conducted extensive work. For example, surface modification has been employed using oxide coating [15–17], conductive substances [18,19], ion doping [20–22], as well as adjusting the composition and structure of the material [23–25]. In the field of lithium-ion battery, the *in-situ* formation of a spinel structure on the surface of lithium-rich layered oxide materials is a strategy that can effectively suppress oxygen loss and structural phase transition during charge and discharge processes, and reduce unfavorable side reactions between the electrode and electrolyte interface [26–28]. This modification method can not only significantly improve the initial Coulombic efficiency and capacity retention rate of the material, but also has a noticeable enhancement effect on cycling performance and rate capability. Therefore, modifying lithium-rich layered oxide materials to form heterostructures is considered one of the most effective ways to enhance its electrochemical performance. As a highly anticipated typical conductive polymer, conductive polypyrrole (PPy) has demonstrated its unique advantages in multiple fields. Its synthesis process is relatively simple, and it possesses key advantages such as high electrical conductivity, excellent stability, environmental friendliness, and reversible redox properties [29–31]. These electrode materials coated with PPy have shown significant performance improvements in electrochemical tests, further demonstrating the tremendous potential of PPy in electrode material optimization.

In this research work, aiming at the shortcomings of structural degradation and poor rate performance in the process of charging and discharging of lithium-rich layered oxide materials, a modified material with a bulk phase structure of layered phase, a surface layer structure of spinel phase, and a PPy film coated on the outer layer of the particles was skillfully designed on the surface of lithium-rich layered oxide materials by one-step synthesis method. The discharge specific capacity of the LLO@S@P-1Mo sample decays from 232.2 mAh/g to 193.4 mAh/g, with a high capacity retention rate of 83.3%. At current densities of 0.1, 0.2, 0.5, 1, 2, 5, and 10 C, its discharge specific capacities are 308.7, 286, 257, 230, 199, 154, and 116 mAh/g, respectively. In addition, after 200 charge-discharge cycles, the voltage decay of LLO@S@P-1Mo is only 0.27 V. Meanwhile, it is also observed that the diffusion coefficient of lithium ions in LLO@S@P-1Mo sample is improved.

In this study, PPy was synthesized *in situ* on the surface of Li-rich layered oxide materials using the oxidation properties of phosphomolybdic acid [32]. Specifically, pyrrole monomers lose an electron under the action of an oxidant and are oxidized to cationic radicals, which then undergo disproportionation to form electrically neutral dipyrrole. This chain reaction continues, sequentially generating dimers, trimers, and ultimately forming a conductive polymer film surrounded by chain-like PPy on the surface of lithium-rich layered oxides (Fig. 1a). Although calcination can cause the decomposition of a small amount of previously synthesized PPy, this loss can be compensated by increasing the amount of PPy synthesis.

To further study the changes of surface morphology of Li-rich layered oxide materials before and after modification, field emission scanning electron microscopy (FE-SEM) and energy dispersive X-ray spectroscopy (EDS) were used to characterize the electrode materials in detail. Figs. 1b–g present the scanning electron microscopy (SEM) images of LLO, LLO@P (before annealing), and LLO@S@P-1Mo (after annealing). The SEM images of more sample particles are shown in Fig. S1 (Supporting information). Through comparative analysis, it can be clearly observed that the surface of LLO exhibits numerous protrusions formed by particle agglomeration, resulting in an irregular structure created by the aggregation of primary particles into larger ones. In contrast, the surfaces of both LLO@P and LLO@S@P-1Mo display a noticeable and relatively smooth coating of PPy film, as shown in regions I and II of Figs. 1f and g. It can be seen from the pictures that the SEM images reveal areas where the PPy film on the particle surface appears fractured. This is due to the prolonged ultrasonic treatment applied to the samples prior to morphological testing, which was intended to partially detach the PPy film in some regions, allowing for a clearer distinction between LLO and the PPy coating. The results demonstrate successful polymerization of pyrrole on the surface of LLO particles, forming a complete and uniform layer of PPy coating.

Fig. 1h illustrates the elemental mapping images obtained through energy-dispersive X-ray spectroscopy (EDS) for LLO@S@P-1Mo. In these images, the distribution of carbon (C) and nitrogen (N) elements, which are the main constituent elements of PPy,

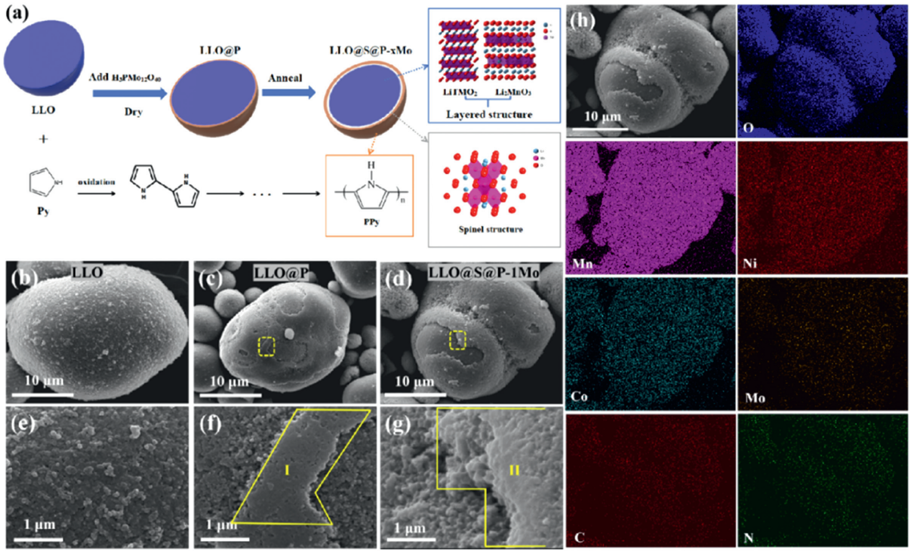

Fig. 1. (a) Schematic diagram of LLO@S@P-xMo. SEM images of (b, e) LLO, (c, f) LLO@P, and (d, g) LLO@S@P-1Mo. (h) EDS mappings of the O, Mn, Ni, Co, Mo, C and N element for LLO@S@P-1Mo.

provides compelling evidence for the presence of PPy. Specifically, Fig. 1h clearly demonstrate the uniform distribution of C and N elements across the material surface, strongly indicating that PPy is fully and evenly coated on the LLO surface. To further elucidate the existence of the PPy coating layer, a detailed analysis of C and N elements was conducted for both the surface PPy coating and the inner LLO component (Fig. S2 in Supporting information). The analytical data reveals that the C and N element content in the LLO component is significantly lower than that in the surface PPy coating layer, further confirming the presence of the PPy coating.

During the synthesis of PPy, a H^+-Li^+ substitution reaction occurs between the dissociated H^+ from phosphomolybdic acid and the surface layer structure of LLO, resulting in the formation of Li vacancy within the material. This crucial step facilitates the structural transformation of the material from a layered to a spinel phase during the subsequent sintering process [33], as shown in Fig. 1a. To further confirm the existence of the PPy film and spinel structure on the surface of LLO, high-resolution transmission electron microscopy (HRTEM) was utilized in this study to conduct an in-depth microstructural analysis of both LLO and LLO@S@P-1Mo materials. Fig. 2 presents the HRTEM images of the LLO@S@P-1Mo material. The observations reveal that the surface of LLO@S@P-1Mo is indeed encapsulated by a layer of amorphous material, which is a typical characteristic of PPy films (Figs. 2b and c). Furthermore, in some edge regions with lattice orientation, two sets of lattice fringes with different interplanar spacings were observed. The interplanar spacing within the crystal is 0.482 nm, corresponding to the (003) plane of the layered structure, as indicated in region 1 of Fig. 2d. In the outer region, these distinct lattice fringes exhibit an interplanar spacing of 0.210 nm, which perfectly matches the lattice spacing of the (400) plane of the spinel phase, as shown in region 2 of Fig. 2d. Additionally, Fig. S3 (Supporting information) displays the HRTEM images of the LLO material. It can be clearly observed that the LLO particles exhibit typical layered structure characteristics, which extend from the interior of the crystal to the surface of the material. Within the LLO crystal, the measured interplanar spacing is 0.479 nm, which is consistent with the (003) plane of the layered structure. These findings provide direct and compelling evidence for the existence of both the PPy film and spinel structure on the surface of the LLO@S@P-1Mo material.

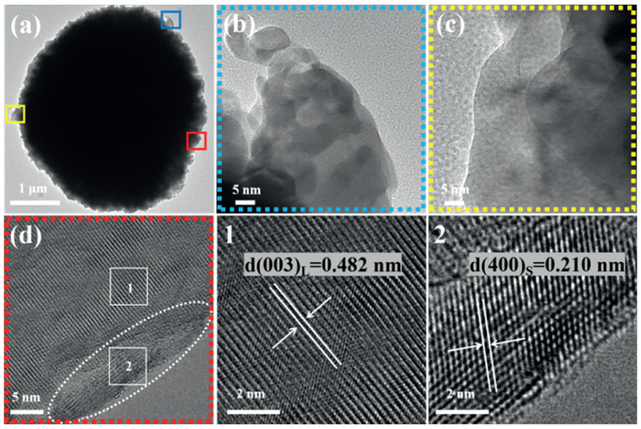

Fig. 2. (a–d) TEM images of LLO@S@P-1Mo sample.

In order to better understand the surface structure changes of Li-rich layered oxide materials, X-ray diffraction (XRD) and Raman spectroscopy were used for detailed analysis. The XRD patterns of the obtained LLO and LLO@S@P-1Mo samples are presented in Fig. 3a. When compared with the standard card (Fig. 3b), it is evident that the patterns of both LLO and LLO@S@P-1Mo exhibit similar characteristic peaks, with most of them attributable to a rhombohedral structure (R-3 m, α-$NaFeO_2$). Additionally, weak diffraction peaks in the range of 20° to 25° originate from Li_2MnO_3 (C2/m space group) [34]. However, in the XRD pattern of LLO@S@P-1Mo, corresponding diffraction peaks belonging to the spinel structure are not clearly observed (Fig. 3c). This could be attributed to the low content and poor crystallinity of the spinel structure, making it difficult to detect the related diffraction peaks [35].

Fig. 3d displays the Raman spectra of LLO and LLO@S@P-1Mo samples. In the Raman spectrum of LLO@S@P-1Mo, the main peaks are located at 490 and 605 cm^{-1}, which can be attributed to A_{1g}

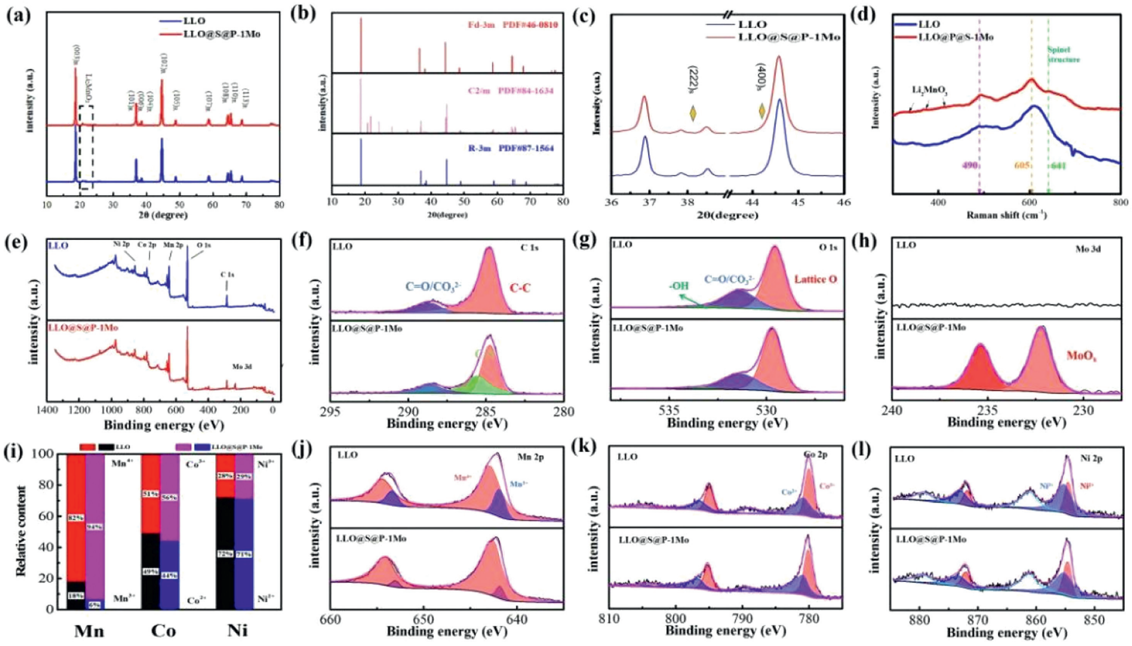

Fig. 3. (a, c) XRD patterns of LLO and LLO@S@P-1Mo. (b) XRD standard card pattern, and (d) Raman spectra of LLO and LLO@S@P-1Mo. (e) XPS spectra of LLO and LLO@S@P-1Mo. High-resolution XPS spectra of (f) C 1s, (g) O 1s, (h) Mo 3d, (j) Mn 2p, (k) Co 2p, and (l) Ni 2p. (i) Relative contents of Ni, Co and Mn.

stretching vibrations, such as bending vibrations in the layered R-3 m structure. Other peaks (approximately 335, 370, 415 cm^{-1}) correspond to phonon vibrations of Li_2MnO_3 [36]. More importantly, a weak and inconspicuous peak appears at approximately 641 cm^{-1} in the Raman spectrum of LLO@S@P-1Mo, which can be ascribed to symmetric Mn-O stretching vibrations in MnO_6 octahedra in the spinel phase [37]. This result provides strong evidence indicating the presence of an induced spinel structure on the surface of the LLO@S@P-1Mo sample.

In summary, XRD and Raman spectroscopy show that during the PPy synthesis process, the dissociation of phosphomolybdic acid and subsequent H^+-Li^+ substitution reactions promote a structural transformation of the material from a layered to a spinel phase to some extent. Although diffraction peaks corresponding to the spinel structure are not clearly observed in the XRD pattern, the results from Raman spectroscopy provide conclusive evidence for its existence.

X-ray photoelectron spectroscopy (XPS) analysis was applied to deeply investigate the surface elemental chemical valence states and bonding configurations of LLO and LLO@S@P-1Mo. By analyzing the high-resolution XPS spectra of C 1s, O 1s, Mo 3d, Mn 2p, Co 2p, and Ni 2p for both LLO and LLO@S@P-1Mo (Figs. 3f–h and j-l) the surface chemical state of the sample can be more accurately revealed. Firstly, Fig. 3e displays the XPS full spectra of LLO and LLO@S@P-1Mo, providing comprehensive elemental information for subsequent detailed analysis. The C 1s spectrum (Fig. 3f) primarily exhibits two bonding states in LLO: C–C and $C{=}O/CO_3^{2-}$ with binding energies of 284.76 and 288.71 eV [38], respectively. In LLO@S@P-1Mo, apart from these two bond types, a distinct C–N peak is observed at a binding energy of 286.17 eV, attributed to the introduction of PPy in the modified sample [39]. Further analysis of the O 1s spectrum (Fig. 3g) reveals the presence of three oxygen-containing valence states corresponding to lattice oxygen, $C{=}O/CO_3^{2-}$, and –OH with binding energies of 529.54, 531.29, and 533.62 eV, respectively. In the Mo 3d spectrum (Fig. 3h), LLO@S@P-1Mo exhibits a typical Mo 3d characteristic peak at a binding energy of 232.23 eV [40], further confirming the role of phosphomolybdic acid in the material synthesis process. For the analysis of transition metal elements, the high-resolution XPS spectrum of Mn 2p in Fig. 3j reveals the presence of Mn^{3+} and Mn^{4+} with binding energies of 641.86 and 642.87 eV, respectively. Similarly, the fitting results of Co $2p_{3/2}$ (Fig. 3k) indicate the existence of Co^{3+} and Co^{2+} with binding energies of 779 and 780.4 eV, respectively. In the spectrum of Ni $2p_{3/2}$ (Fig. 3l), it can be concluded that the contributions of Ni^{2+} and Ni^{3+} with binding energies of 854.47 and 855.1 eV, respectively, accompanied by a Ni^{2+} satellite peak at 861.17 eV [41,42].

It is noteworthy that although XPS signal intensity (*i.e.*, peak area) is often used to infer the relative content of elements, considering various complex factors that may affect signal intensity, XPS data can only be used as a semi-quantitative basis for element analysis. Even so, it is evident from Fig. 3i that compared to LLO, the relative contents of surface transition elements Co^{2+}, Co^{3+}, Ni^{2+}, and Ni^{3+} on LLO@S@P-1Mo remain almost unchanged, while the relative content of Mn^{4+} increases significantly. This change can be attributed to the oxidation effect of phosphomolybdic acid, which enhances the average valence state of surface transition elements in the material. In particular, the change in Mn element valence state is believed to be beneficial for the formation of spinel phases $Li_4Mn_5O_{12}/LiMn_{1.5}Ni_{0.5}O_4$, further confirming the existence of a spinel structure on the material surface [43].

Fig. 4a illustrates the relationship between specific discharge capacity and cycle number for LLO, LLO@S@P-0.5Mo, LLO@S@P-1Mo, and LLO@S@P-2Mo samples at 1 C. Correspondingly, Figs. 4b and c depict the initial charge-discharge curves of LLO and LLO@S@P-1Mo at 1 C. As observed from the figures, after 200 cycles, the specific discharge capacity of the LLO sample decreased from an initial value of 229.8–172.9 mAh/g. In contrast, the specific discharge capacity of LLO@S@P-0.5Mo, LLO@S@P-1Mo, and LLO@S@P-2Mo samples decreased from 208.9, 232.2, and 251.3 mAh/g to 188, 193.4, and 168.6 mAh/g, respectively. Accordingly, their capacity retention rates were 75.2%, 90%, 83.3%, and 67.1%, respectively. The specific discharge capacity of LLO and LLO@S@P-1Mo samples at 1 C changes with the number of cycles (Fig. S4 in Supporting information). Through surface modification, the capacity retention rates of the modified samples were significantly enhanced, demonstrating excellent electrochemical performance. This improvement was mainly attributed to two factors: Firstly, the spinel structure effectively alleviated oxygen loss, thus suppressing the phase transformation of LLO and ensuring good electrochemical stability [27]. Secondly, the existence of spinel structure and PPy film provides a protective effect of core-shell structure during the cycling process, which further inhibits the side reactions between layered structure and electrolyte [39]. These combined factors contributed to the outstanding electrochemical performance of the modified samples.

Fig. 4d presents the cyclic rate performance of batteries assembled with LLO, LLO@S@P-0.5Mo, LLO@S@P-1Mo, and LLO@S@P-2Mo samples at different current densities. Figs. 4e and f show the discharge curves of LLO and LLO@S@P-1Mo at various current densities, respectively. As observed from the figures, the specific discharge capacities of the LLO material at current densities of 0.1, 0.2, 0.5, 1, 2, 5, and 10 C were 280, 264, 240, 217, 188, 140, and 94 mAh/g, respectively. In comparison, the specific discharge capacities of the LLO@S@P-1Mo material battery at these current densities were 309, 286, 257, 230, 199, 154, and 116 mAh/g, respectively, indicating that LLO@S@P-1Mo had a higher specific discharge capacity than LLO at all current densities tested. These results demonstrate that after composite modification with the spinel structure and PPy film, the LLO@S@P-1Mo sample exhibited a higher discharge capacity at different rates, thus exhibiting superior rate performance. This improvement can be attributed to the properties of the spinel structure, which acts as a fast lithium-ion conductor and can effectively increase the diffusion rate of lithium ions in the charged and discharged state [36]. Meanwhile, as an excellent electronic conductor, the PPy film can significantly enhance the conduction rate of electrons [44]. Therefore, under the synergistic effect of the spinel structure and PPy film, the rate performance of sample was significantly improved.

Fig. 4g presents the cyclic voltammetry (CV) curve for the first cycle of LLO and LLO@S@P-1Mo. While both materials showed high similarity in shape, closer inspection revealed an additional peak at 3.0/2.85 V for LLO@S@P-1Mo, attributed to the emergence of the spinel phase. Fig. 4h further illustrates the CV curves for the first three cycles of LLO@S@P-1Mo. The peak near 3.9 V corresponds to the oxidation of Ni^{2+} and Co^{3+} to higher valence states (Ni^{3+}, Ni^{4+}, and Co^{4+}), accompanied by the extraction of Li^+ from $LiMO_2$. The peak at 4.6 V is associated with the activation process of Li_2MnO_3, which involves irreversible oxygen loss [45]. Notably, the specific redox peaks exhibited by LLO@S@P-1Mo at 3.0/2.85 V, as evident from the figures, indicate a reversible transformation process due to their consistent position and intensity [46]. Figs. 4j and k depict the dQ/dV curves of LLO and LLO@S@P-1Mo at different cycles at 1 C. As the cycles progressed, a gradual shift of the reduction peaks towards lower potentials was observed for both LLO and LLO@S@P-1Mo, with a stable reduction peak forming at approximately 2.75 V. This shift indicates a structural transformation from a layered to a spinel structure. Notably, LLO@S@P-1Mo retained a distinct reduction peak near 3.2 V even after multiple cycles, suggesting the preservation of more layered structure characteristics [47]. Hence, it can be inferred that LLO@S@P-1Mo exhibits a more stable layered structure. Fig. 4i portrays the relationship between average

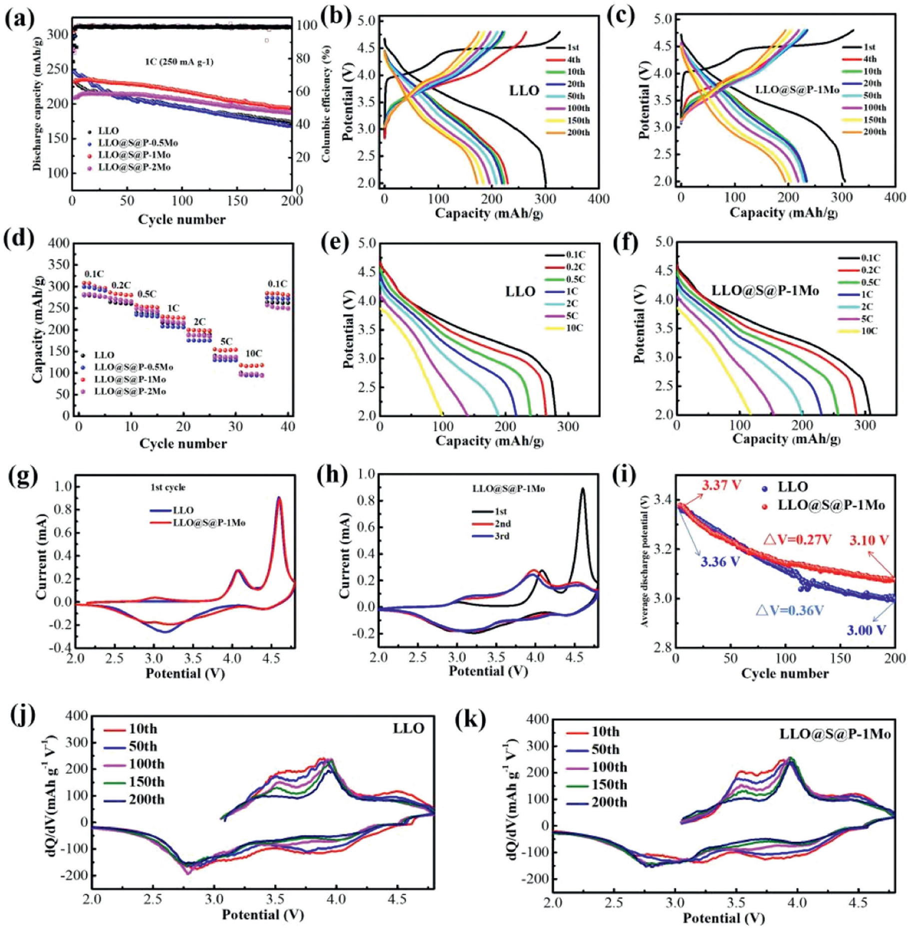

Fig. 4. (a) Cycling performance of LLO, LLO@S@P-0.5Mo, LLO@S@P-1Mo, and LLO@S@P-2Mo at 0.1 C (1st) and 1 C. Initial charge-discharge curves of (b) LLO and (c) LLO@S@P-1Mo at 0.1 C (1st) and 1 C. (d) Rate capabilities of LLO, LLO@S@P-0.5Mo, LLO@S@P-1Mo, and LLO@S@P-2Mo. Discharge curves of (e) LLO and (f) LLO@S@P-1Mo at current densities of 0.1, 0.2, 0.5, 1, 2, 5, and 10 C. (g) First cycle voltammogram of LLO and LLO@S@P-1Mo. (h) First three cycle voltammograms of LLO@S@P-1Mo. (i) Relationship between average discharge voltage and cycle number of LLO and LLO@S@P-1Mo. d*Q*/d*V* plots of (j) LLO and (k) LLO@S@P-1Mo in different charge and discharge cycles.

discharge voltage and cycle number for LLO and LLO@S@P-1Mo at a 1 C current density. After 200 cycles, the average discharge voltages of LLO and LLO@S@P-1Mo decreased by 0.36 V and 0.27 V, respectively. Evidently, through spinel coating modification, the voltage decay of the LLO cathode was significantly mitigated, further confirming the effectiveness of modification in enhancing the electrochemical performance of the material.

To further investigate the impact of the spinel structure and PPy film on the performance of the LLO cathode, electrochemical impedance spectroscopy (EIS) tests were conducted using an electrochemical workstation (Zahner Zennium). Measurements were taken after the 4th, 10th, and 50th cycles of the battery charged to 4.0 V. The resulting Nyquist plots are presented in Figs. 5a–c. It can be observed from the figures that the EIS spectra of all samples consist of a semicircle in the high-frequency region, a semicircle in the mid-frequency region, and a straight line in the low-frequency region. In the Nyquist plot, the intersection of the high-frequency region with the real axis is typically regarded as the ohmic resistance (R_s) of the cell. The semicircle in the high-frequency region represents the impedance (R_{sf}) related to the diffusion migration of Li^+ through the cathode electrolyte interface (CEI) film, while the semicircle in the mid-frequency region corresponds to the impedance (R_{ct}) associated with charge transfer. The straight line in the low-frequency region reflects the solid-state diffusion impedance of Li^+ within the active material, which can be represented by the Warburg impedance (Z_W) that describes diffusion [48]. The electrochemical model of AC impedance is shown in Fig. S5 (Supporting information).

Figs. 5d–f depict the impedance parameter plots corresponding to Figs. 5a–c. It is evident from these figures that the R_{sf} values of the LLO@S@P-1Mo samples are smaller than those of the LLO cathode. This difference is attributed to the PPy film on the surface of the LLO@S@P-1Mo samples, which effectively suppresses side reactions with the electrolyte, resulting in a thinner and more stable CEI film. Therefore, compared to LLO, the LLO@S@P-1Mo samples exhibit lower Li^+ transfer resistance. Additionally, it is noteworthy that the R_{ct} values of the LLO@S@P-1Mo samples are also smaller than those of the LLO samples. Changes in R_{ct} are closely related to phase transitions within the material, reflecting the structural stability of the active material during cycling. This suggests that the spinel structure can alleviate phase transitions during the reaction process, maintaining the stability of the crystal structure and ultimately enhancing the cycling stability of LLO [49]. These results provide valuable insights into how the spinel structure and PPy film improve the performance of the LLO cathode.

The diffusion rate of lithium ions plays a crucial role in the electrode materials of lithium-ion batteries, exerting a direct and profound influence on the rate capability of the batteries. In order to thoroughly investigate the specific effects of spinel and PPy components on the diffusion coefficient of lithium ions, the behavior of LLO and LLO@S@P-1Mo samples during the second charge and discharge cycle was measured in detail using the Galvanostatic

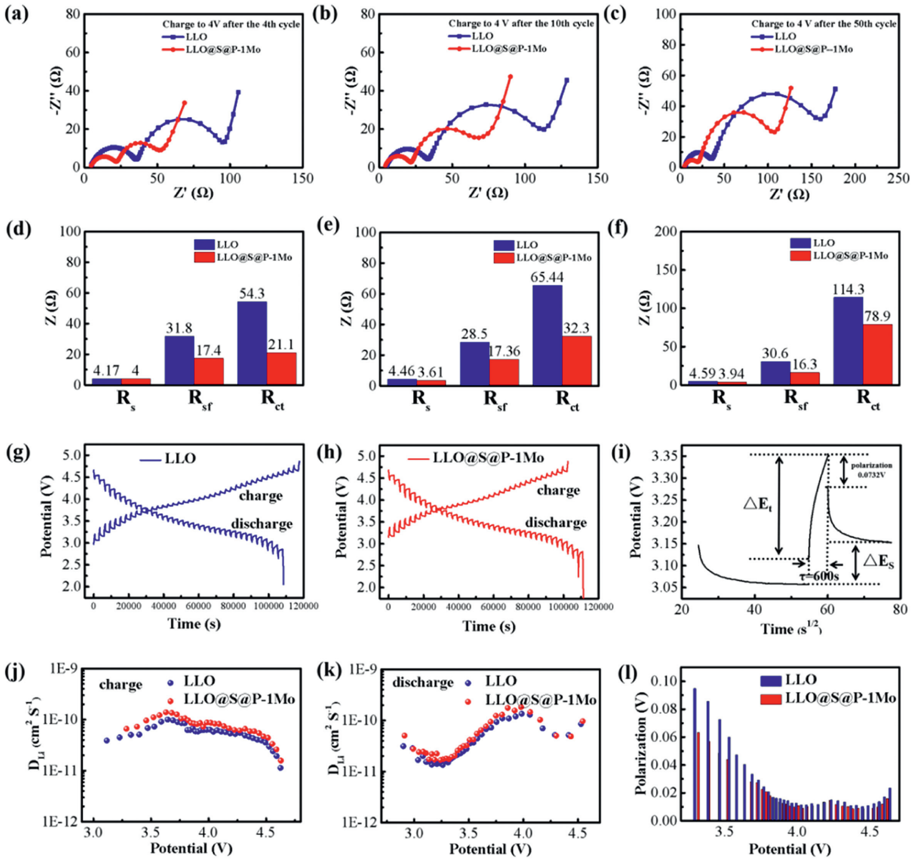

Fig. 5. Nyquist plots of LLO and LLO@S@P-1Mo after (a) 4, (b) 10, and (c) 50 cycles at 1 C, and (d-f) their corresponding impedance parameters. GITT curves of (g) LLO and (h) LLO@S@P-1Mo during the second charge-discharge process (0.2 C). (i) Single titration GITT curve. (j, k) Li^+ diffusion coefficient during charge and discharge process obtained from GITT test. (l) Distribution diagram of polarization voltage with voltage change.

Intermittent Titration Technique (GITT) method [34]. Figs. 5g and h show the charge and discharge GITT curves for LLO and LLO@S@P-1Mo samples. During the titration process, a constant current of 0.2 C was used for 10 min of charge and discharge, followed by a 30-min rest before the next charge and discharge. This process was continued until the voltage reached 4.8 V or 2.0 V, respectively. As clearly observed in Fig. 5i, there is a definite linear relationship between the square root of titration time and voltage. Combining GITT testing with corresponding data calculations, the relationship curves between lithium-ion diffusivity and charge potential can be obtained (Figs. 5j and k). It is evident from the GITT data that the lithium-ion diffusion coefficient of the LLO@S@P-1Mo sample is higher than that of the LLO sample, with maximum values of 1.388×10^{-10} and 1.004×10^{-10} cm^2/s, respectively. This result provides a compelling explanation for its superior rate performance.

Additionally, Fig. 5l reveals the polarization phenomenon during the charging process for both LLO and LLO@S@P-1Mo samples. The results show that the polarization rate of the LLO@S@P-1Mo sample is lower than that of the LLO sample. The GITT experiments strongly demonstrate the excellent electrochemical performance of the LLO@S@P-1Mo sample in terms of rapid lithium-ion diffusion and low electrode ohmic polarization. The significant improvement in lithium-ion diffusivity for the LLO@S@P-1Mo sample may be closely related to the presence of a layered spinel structure.

In this paper, the acidity and oxidation properties of phosphomolybdic acid are skillfully utilized to prepare a modified lithium-rich layered oxide materials with a composite structure through an innovative method. This material possesses characteristics of both layered and spinel phases, as well as particles coated with a PPy film. This composite structure not only significantly mitigates structural degradation issues during the layered-to-spinel phase transition in lithium-rich layered oxide materials during charge and discharge processes, but also protects the electrode materials from the erosion of the electrolyte. Through comprehensive evaluation of the electrochemical performance of the modified material, it was found that the LLO@S@P-1Mo modified sample can maintain a high specific discharge capacity of 193.4 mAh/g after 200 cycles at a current density of 1 C, with an improved capacity retention rate of 83.3% and a voltage attenuation of only 0.27 V. It is worth mentioning that the lithium ion diffusion coefficient and rate performance of the modified sample are also improved. This method provides a new solution strategy for protecting lithium-rich layered oxide materials during long-term charge and discharge processes and opens up new avenues for the development of high-performance lithium-ion batteries.

Declaration of competing interest

The authors declare that they have no known competing financial interests or personal relationships that could have appeared to influence the work reported in this paper.

CRediT authorship contribution statement

Bing Jiang: Methodology, Writing – original draft, Writing – review & editing. **Gang Zou:** Methodology, Writing – original draft, Writing – review & editing. **Bi Luo:** Writing – review & editing. **Yan Guo:** Validation. **Jingru Li:** Methodology. **Wendi Zhang:**

Methodology. **Qianxiao Fan:** Data curation. **Lehao Liu:** Methodology. **Lihua Chu:** Methodology. **Qiaobao Zhang:** Methodology, Supervision. **Meicheng Li:** Funding acquisition, Methodology, Project administration, Supervision, Writing – review & editing.

Acknowledgments

This work is supported partially by projects of National Natural Science Foundation of China (Nos. 52272200, 51972110, 52102245, 52102203 and 52072121), State Key Laboratory of Alternate Electrical Power System with Renewable Energy Sources (Nos. LAPS21004, LAPS202114), Beijing Natural Science Foundation (Nos. 2222076, 2222077), Hebei Natural Science Foundation (No. E2022502022), Huaneng Group Headquarters Science and Technology Project (No. HNKJ20-H88), 2022 Strategic Research Key Project of Science and Technology Commission of the Ministry of Education, China Postdoctoral Science Foundation (No. 2022M721129) and the Fundamental Research Funds for the Central Universities (Nos. 2022MS030, 2021MS028, 2020MS023, 2020MS028) and the NCEPU "Double First-Class" Program.

Supplementary materials

Supplementary material associated with this article can be found, in the online version, at doi:10.1016/j.cclet.2024.109801.

References

[1] Y. Gao, Z. Pan, J. Sun, et al., Nano-Micro Lett. 14 (2022) 1–49.
[2] M. Jung, S. Schwunk, Green 3 (2013) 19–26.
[3] Z.P. Cano, D. Banham, S. Ye, et al., Nat. Energy 3 (2018) 279–289.
[4] J. Wang, X. He, E. Paillard, et al., Adv. Energy Mater. 6 (2016) 1600906.
[5] L. Xu, S. Chen, Y. Su, et al., Energy Mater. Adv. 4 (2023) 45.
[6] M.M. Thackeray, S.H. Kang, C.S. Johnson, et al., J. Mater. Chem. 17 (2007) 3112–3125.
[7] E.Y. Hu, X.Q. Yu, R.Q. Lin, et al., Nat. Energy 3 (2018) 690–698.
[8] L. Xu, S. Chen, Y. Su, et al., ACS Appl. Mater. Interfaces 15 (2023) 54559–54567.
[9] K. Shimoda, T. Minato, K. Nakanishi, et al., J. Mater. Chem. A: Mater. Energy Sustain. 4 (2016) 5909–5916.
[10] N. Charles, Y. Yu, L. Giordano, et al., Chem. Mater. 32 (2020) 5502–5514.
[11] A. Singer, M. Zhang, S. Hy, et al., Nat. Energy 3 (2018) 641–647.
[12] D.H. Seo, J. Lee, A. Urban, et al., Nat. Chem. 8 (2016) 692–697.
[13] F. Dogan, B.R. Long, J.R. Croy, et al., J. Am. Chem. Soc. 137 (2015) 2328.
[14] H. Koga, L. Croguennec, M. Ménétrier, et al., J. Power Sources 236 (2013) 250–258.
[15] G. Kobayashi, Y. Irii, F. Matsumoto, et al., J. Power Sources 303 (2016) 250–256.
[16] Y.J. Zhao, Z. Lv, T. Xu, J.X. Li, J. Alloys Compd. 715 (2017) 105–111.
[17] W. Liu, X. Zhang, C. Li, et al., Chin. Chem. Lett. 31 (2020) 2225–2229.
[18] Y. Li, X. Zhu, C. Wei, et al., Chin. Chem. Lett. 35 (2024) 109536.
[19] Y. Li, X. Zhu, Y. Su, et al., Small 20 (2024) 2307292.
[20] C. Song, C. Zhuo, X. Min, et al., ACS Appl. Energ. Mater. (2018) 8b-740b.
[21] J. Billaud, D. Sheptyakov, S. Sallard, et al., J. Mater. Chem. A 7 (2019) 15215–15224.
[22] R. Yue, F. Xia, R. Qi, et al., Chin. Chem. Lett. 32 (2021) 849–853.
[23] H.X. Wei, Y.D. Huang, L.B. Tang, et al., Nano Energy (2021) 106288.
[24] L. Li, P. Ji, M. Huang, et al., Chin. Chem. Lett. 35 (2024) 109144.
[25] L. Li, Y. Chen, Y. Liu, et al., Rare Metals 42 (2023) 830–837.
[26] J. Zhang, R. Gao, L. Sun, et al., Phys. Chem. Chem. Phys. 18 (2016) 25711–25720.
[27] H. Xie, J. Cui, Z. Yao, et al., Chem. Eng. J. 427 (2022) 131978.
[28] B. Zhao, L. Ma, K. Wu, et al., Chin. Chem. Lett. 32 (2021) 125–131.
[29] G.X. Wang, L. Yang, Y. Chen, et al., Electrochim. Acta 50 (2005) 4649–4654.
[30] S.Y. Chew, Z.P. Guo, J.Z. Wang, et al., Electrochem. Commun. 9 (2007) 941–946.
[31] S. Jia, W. Xu, Y. Chen, et al., Chin. Chem. Lett. 32 (2021) 2773–2776.
[32] C. Marchal-Roch, J.M. Millet, Comptes Rendus De L'académie Des Sciences - Series IIC - Chemistry 4 (2001) 321–329.
[33] G. Zhang, M. Chen, C. Li, et al., Chem. Eng. J. 443 (2022) 136434.
[34] Z. Yu, Q. Lu, Y. Wang, et al., Appl. Surf. Sci. 619 (2023) 156683.
[35] X. Ding, D. Luo, J. Cui, et al., Angew. Chem. Int. Ed. 59 (2020) 7778–7782.
[36] P. Zhang, X. Zhai, H. Huang, et al., J. Power Sources 499 (2021) 229966.
[37] J. Zhao, R. Huang, W. Gao, et al., Adv. Energy Mater. 5 (2015) 1401937.
[38] W. Li, B. Zhao, J. Bai, et al., Chem. Eng. J. 454 (2023) 140398.
[39] S.Y. Kim, C.S. Park, S. Hosseini, et al., Adv. Energy Mater. 11 (2021) 2100552.
[40] H. Zhu, H. Yu, H. Jiang, et al., Chem. Eng. Sci. 217 (2020) 115518.
[41] M. Li, X. Deng, Z. Wang, et al., Appl. Surf. Sci. 592 (2022) 153328.
[42] N. Hu, C. Zhang, K. Song, et al., Chem. Eng. J. 415 (2021) 129042.
[43] S. Ivanova, E. Zhecheva, D. Nihtianova, et al., J. Mater. Sci. 46 (2011) 7098–7105.
[44] X. Wang, L. Xu, Y. Chang, et al., J. Solid State Electrochem. 27 (2023) 1459–1467.
[45] M. Cai, Z. Huang, Y. Huang, et al., Ceram. Int. 47 (2021) 9551–9559.
[46] J. Karunawan, O. Floweri, S.P. Santosa, et al., J. Electroanal. Chem. 907 (2022) 116050.
[47] H. Wei, Y. Huang, L. Tang, et al., Nano Energy 88 (2021) 106288.
[48] K. Pan, F. Zou, M. Canova, et al., J. Power Sources 479 (2020) 229083.
[49] J. Feng, Y. Jiang, F. Yu, et al., J. Energy Chem. 66 (2022) 666–675.